


 CrossMark  
 click for updates
Cite this: *Nanoscale*, 2014, 6, 10394

# WS<sub>2</sub> nanosheet as a new photosensitizer carrier for combined photodynamic and photothermal therapy of cancer cells†

 Yuan Yong,<sup>‡a</sup> Liangjun Zhou,<sup>‡ac</sup> Zhanjun Gu,<sup>\*a</sup> Liang Yan,<sup>a</sup> Gan Tian,<sup>ad</sup>  
 Xiaopeng Zheng,<sup>ac</sup> Xiaodong Liu,<sup>e</sup> Xiao Zhang,<sup>ab</sup> Junxin Shi,<sup>af</sup> Wenshu Cong,<sup>a</sup>  
 Wenyan Yin<sup>\*a</sup> and Yuliang Zhao<sup>\*ab</sup>

We have developed a simple and efficient strategy to fabricate WS<sub>2</sub> nanosheets with low toxicity and good water solubility via a liquid exfoliation method by using H<sub>2</sub>SO<sub>4</sub> intercalation and ultrasonication. The as-prepared WS<sub>2</sub> nanosheets were employed not only as an NIR absorbing agent for photothermal therapy (PTT) but also as a photosensitizer (PS) carrier for photodynamic therapy (PDT) due to their sheet like structure that offers large surface area to load PS molecules. Moreover, singlet-oxygen generation of the PSs–WS<sub>2</sub> complex could be finely controlled by NIR irradiation that could manipulate the PSs release behavior from WS<sub>2</sub> nanosheets. The synergistic anti-tumor effect of WS<sub>2</sub> nanosheets mediated PDT–PTT was also evaluated carefully and the results clearly showed that the efficacy of combined PDT–PTT treatment of cancer cells is significantly higher than those of PDT-only and PTT-only treatment, indicating enhanced efficiency of the combined therapeutic system. In addition, the WS<sub>2</sub> could be used as a computed tomography (CT) contrast agent for bio-imaging since W atoms have strong X-ray attenuation ability, making them a multifunctional theranostic platform for simultaneous imaging-guided diagnosis and therapy.

 Received 6th May 2014  
 Accepted 13th June 2014

DOI: 10.1039/c4nr02453b

www.rsc.org/nanoscale

## Introduction

Phototherapy, including photothermal and photodynamic therapy, has increasingly attracted much attention for the treatment of various cancers due to its many advantages such as low cost, highly localized and specific tumor treatment, fewer side effects compared with radiation therapy and chemotherapy, outpatient therapy and minimal trauma to tissues.<sup>1</sup> This type of therapy used photosensitizers (PSS) and light irradiation to eradicate target tumors. For photothermal therapy (PTT), the photosensitizer is usually a kind of optical absorbing

agent with strong near infrared (NIR) absorbance that has the capability to efficiently convert photo-energy into heat to kill cancer cells under NIR irradiation.<sup>2,3</sup> While, in the process of photodynamic therapy (PDT), the photo-energy could be transferred from photosensitizers to the surrounding oxygen molecules, resulting in the generation of cytotoxic oxygen-based molecular species such as <sup>1</sup>O<sub>2</sub> to induce cell death and tissue destruction.<sup>4,5</sup> Recently, the emergence of nanomaterials has offered new opportunities to improve the therapeutic efficacy or overcome the limitations in the current PTT and PDT.<sup>6–10</sup> For example, PS molecules for PDT are usually composed of lipophilic compounds that show poor water solubility, resulting in the aggregation of PS molecules in blood plasma. Nanoscaled materials could be used as efficient PS carriers to facilitate the delivery of PSs due to their better hydrophilicity and appropriate size for passively targeting tumor tissues through the enhanced permeability and retention effects (EPR).<sup>11–17</sup> Some nanomaterials such as gold nanoparticles,<sup>18–26</sup> carbon nanomaterials<sup>27–30</sup> and copper sulfide,<sup>31–36</sup> have been widely employed as PTT agents, which could efficiently convert the light into heat and thus induce hyperthermia to tumor tissues without damaging adjacent healthy tissues, showing reduced side effects and improved selectivity. Although impressive advances have been made in nanoscale PS agents for PTT and PDT, the types of nanomaterials combining both PDT and PTT capabilities simultaneously are limited. Combined

<sup>a</sup>Key Laboratory for Biomedical Effects of Nanomaterials and Nanosafety, Institute of High Energy Physics, Chinese Academy of Sciences, Beijing, 100049, P. R. China. E-mail: zjgu@ihep.ac.cn; zhaoyuliang@ihep.ac.cn; yinwy@ihep.ac.cn

<sup>b</sup>Key Laboratory for Biomedical Effects of Nanomaterials and Nanosafety, National Center for Nanosciences and Technology of China, Beijing, 100190, P. R. China

<sup>c</sup>College of Materials Science and Opto-Electronic Technology, University of Chinese Academy of Sciences, Beijing, 100049, P. R. China

<sup>d</sup>College of Chemistry, Sichuan University, Chengdu, 610064, P. R. China

<sup>e</sup>College of Environmental and Chemical Engineering, Yanshan University, Qinhuangdao, 066004, P. R. China

<sup>f</sup>Department of Material Physics & Chemistry, College of Materials Science & Engineering, Huaqiao University, Xiamen 361021, P. R. China

† Electronic supplementary information (ESI) available. See DOI: 10.1039/c4nr02453b

‡ These authors contributed equally.

phototherapies (PDT and PTT) based on one nanoplatform may exceed the individual therapeutic efficacy of each system and lead to enhanced therapeutic outcome.<sup>37–42</sup> Therefore, there is still a great demand for developing new nanomaterials for combined photodynamic and photothermal therapy to realize synergistic anti-cancer effects.

Very recently, two-dimensional (2D) nanoscaled transition-metal dichalcogenides, such as MoS<sub>2</sub> and WS<sub>2</sub>, have been used as new NIR absorbing agents for PTT ablation of cancer *in vitro* and *in vivo*.<sup>43–45</sup> For example, in the latest report, Liu *et al.* have for the first time demonstrated the potential of WS<sub>2</sub> in highly effective *in vivo* photothermal ablation of tumors in a mouse model.<sup>43</sup> Moreover, since tungsten has the strong X-ray attenuation ability, the application of WS<sub>2</sub> nanosheets could also extend to be used as an X-ray computed tomography (CT) contrast agent for bio-imaging of tumors.<sup>43</sup> Apart from its potential for PTT and bio-imaging, WS<sub>2</sub> nanosheet may also act as a drug delivery carrier, which is ideal for drug loading through physical interaction or chemical conjugation due to its sheet like structure with a high surface area. Therefore, the WS<sub>2</sub> nanosheet could be an ideal multifunctional platform for simultaneous bio-imaging and combined PDT–PTT therapy of cancer. However, no studies have been reported on WS<sub>2</sub> nanosheets mediated delivery of photosensitizers, and also no research has been carried out to evaluate the synergistic anti-tumor effect of WS<sub>2</sub> nanosheets mediated PDT–PTT.

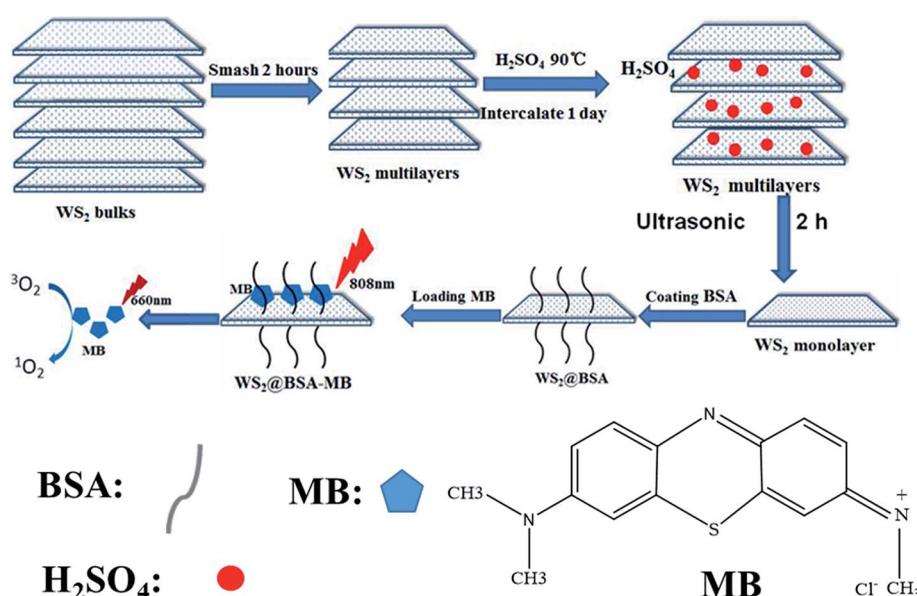
In this work, for the first time, we used BSA-coated WS<sub>2</sub> nanosheets as photosensitizer carriers for combined PDT and PTT. The as-obtained WS<sub>2</sub>–PS complex showed enhanced anti-cancer effects *in vitro* by the combination of photothermal and photodynamic therapy. Interestingly, we also found that the singlet-oxygen generation (SOG) by PSs could be effectively controlled by NIR irradiation that could manipulate the PS's

release behavior from WS<sub>2</sub> nanosheets. When PSs (MB) are adsorbed on the surface of WS<sub>2</sub> nanosheets, the energy transfer from PSs to WS<sub>2</sub> is effective, and the SOG could be efficiently inhibited by WS<sub>2</sub> due to its high optical absorption. Upon NIR irradiation, WS<sub>2</sub> converts optical energy to heat, which results in the efficient release of PSs from WS<sub>2</sub> nanosheets. Thus, the efficiency of <sup>1</sup>O<sub>2</sub> production can be remarkably recovered (Scheme 1). This feature makes WS<sub>2</sub> nanosheets a smart platform for the controllable regulation of photo-activity of PSs, which may improve the efficacy and selectivity of phototherapy and reduce the unwanted collateral damage to surrounding normal tissues. Moreover, WS<sub>2</sub> nanosheets also showed strong X-ray attenuation, which provided the potential for CT bio-imaging. Therefore, the as-prepared WS<sub>2</sub> nanosheets offer a new possibility in exploring the multifunctional nano-platform for simultaneous biomedical imaging and combined PDT and PTT.

## Materials and methods

### Materials

Commercial tungsten disulfide (WS<sub>2</sub>, 99.8%), and methylene blue (MB, biological stain) were obtained from Alfa Aesar and used without further purification. Sulfuric acid (H<sub>2</sub>SO<sub>4</sub>, 95.0–98.0%, analytical reagent) was purchased from Beijing Chemical Corporation. Bovine serum albumin (BSA) was obtained from Amersco Company. Singlet Oxygen Sensor Green reagent (SOSG, molecular probe) was supplied by Life Technologies. Dulbecco's Modified Eagle Medium (DMEM) and fetal bovine serum (FBS) were obtained from Gibco. Calcein-AM (CA)–propidium iodide (PI) stain and Cell Counting Kit-8 (CCK-8) were provided by Dojindo Laboratories. Deionized (DI) water was used in the whole process.



**Scheme 1** Schematic illustration of the synthetic procedure of WS<sub>2</sub> nanosheets and their application as a multifunctional photosensitizer delivery system for combined photothermal and photodynamic therapy of cancer.

### Preparation of mono/few layer(s) of WS<sub>2</sub> nanosheets

Commercial WS<sub>2</sub> powder was first ground in a grinding miller for 2 h. Subsequently, the WS<sub>2</sub> (40 mg) powder was dispersed in 40 mL of sulfuric acid (H<sub>2</sub>SO<sub>4</sub>, 95.0–98.0%) for intercalation for 24 h at 90 °C. The as-prepared products were collected by centrifugation and washed with DI water for several times to remove the residual H<sub>2</sub>SO<sub>4</sub>. Then, the H<sub>2</sub>SO<sub>4</sub>-intercalated WS<sub>2</sub> were dispersed into 40 mL of DI water under bath-sonication for 20 min. Finally, the solutions were probe-sonicated at a power of 325 W for 2 h. The mono/few layer(s) WS<sub>2</sub> nanosheets were obtained by centrifugation and washed with DI water. The yield of the as-prepared WS<sub>2</sub> nanosheets is calculated to be 90%.

### Surface modification of WS<sub>2</sub> nanosheets with BSA

To make the synthesized WS<sub>2</sub> nanosheets usable in biological systems, BSA was used to modify the surface of WS<sub>2</sub> nanosheets. In a typical synthesis, 60 mg of BSA was mixed with 3 mL of WS<sub>2</sub> (2 mg mL<sup>-1</sup>) aqueous solution and then stirred for 3 h at room temperature. The as-synthesized BSA-WS<sub>2</sub> nanosheets were collected by centrifugation at 12 000 rpm for 5 min. Finally, the precipitate was re-dispersed in DI water and stored at 4 °C for further experiments.

### Loading and release behaviors of photosensitizer methylene blue

To investigate the MB loading capacity, MB solution at different concentrations (250, 200, 150, 100, 50 and 25 µM) was slowly added into a BSA-WS<sub>2</sub> dispersion and then the mixture was magnetically stirred overnight at room temperature without light irradiation. After that, unloaded MB was removed by centrifugation and washed with DI water. The amount of MB loaded on the BSA-WS<sub>2</sub> nanosheet surface was determined by the change in its characteristic peak absorption at 665 nm using UV-vis spectroscopy.

### Singlet oxygen measurement

In a typical experiment, singlet oxygen sensor green (SOSG), which is highly sensitive to singlet oxygen (<sup>1</sup>O<sub>2</sub>), was employed as a molecular probe to detect the singlet oxygen through fluorescence detection. 2.5 µM of SOSG were mixed with different samples, and then irradiated by 808 nm laser (1 W cm<sup>-2</sup>), 665 nm LED lamp (0.05 W cm<sup>-2</sup>), or both of them used simultaneously for different time periods. The generation of <sup>1</sup>O<sub>2</sub> was measured *via* detecting the increase in intensity of the SOSG photoluminescence (PL) emission band at 530 nm, when using the characteristic peak absorption of SOSG excited at 494 nm.

### NIR laser photothermal effect of WS<sub>2</sub> nanosheets

To investigate the photothermal effect of as-prepared WS<sub>2</sub> nanosheets, different concentrations of WS<sub>2</sub> nanosheets were irradiated by 808 nm NIR laser at a power density of 1 W cm<sup>-2</sup> for 10 min. The temperature of the solution was measured by using an IR thermal camera at each time point. Meanwhile, to evaluate the impact of NIR laser power density, the

concentration of WS<sub>2</sub> was kept at 50 µg mL<sup>-1</sup> while different power densities (1.0, 0.8, 0.5, 0.3 W cm<sup>-2</sup>) were used to irradiate for 10 min, without changing other experimental conditions. DI water was used as a negative control.

### Cytotoxicity evaluation and luminescence microscopy imaging *in vitro*

HeLa cells (Human cervical cancer cells) were chosen and cultured in a 96-well culture plate at a density of 2 × 10<sup>4</sup> per well. The cells were seeded in DMEM (High Glucose) culture medium containing 10% fetal bovine serum (FBS, GIBCO) at 37 °C under a humidified atmosphere with 5% CO<sub>2</sub>. After 24 h incubation, the cells were treated with different concentrations of WS<sub>2</sub> or BSA-WS<sub>2</sub> and co-incubated for another 24 h without light interference. Then the culture medium was removed and cells were washed twice with PBS. Subsequently, 100 µL of fresh DMEM medium containing CCK-8 (10%) was added and further incubated for 1 h at 37 °C, and finally the absorbance of the samples in fresh DMEM was measured at the characteristic peak of 450 nm using the microplate reader (Thermo scientific, MULTISCAN MNK3).

For combining PTT and PDT effects *in vitro*, HeLa cells were incubated in a 6-well culture plate at a density of 2 × 10<sup>4</sup> per well. After that, HeLa cells were treated with BSA-WS<sub>2</sub>, MB or BSA-WS<sub>2</sub>@MB complex for 24 h. The concentration of BSA-WS<sub>2</sub> and MB was fixed at 100 µg mL<sup>-1</sup> and 3.5 µg mL<sup>-1</sup>, respectively. Subsequently, the culture medium was removed and cells were washed twice with PBS and replaced by fresh DMEM medium. Then the cells treated with BSA-WS<sub>2</sub>, MB or BSA-WS<sub>2</sub>@MB complex were irradiated by an 808 nm laser (15 min), 665 nm LED lamp (5 min), or both of them used at the same time. After incubating for 12 h, the culture medium was removed and cells were washed twice with PBS and stained with CA-PI for 15 min, washed twice with PBS again, and then the luminescence images were acquired using an inverted luminescence microscope (OLYMPUS X73, JAPAN).

### CT imaging *in vitro* and *in vivo*

Different concentrations of BSA-WS<sub>2</sub> were dissolved in 0.5% agarose gel solution and set in 1.5 mL centrifuge tubes for further phantom tests. Iopromide at the same concentrations as BSA-WS<sub>2</sub> was used as the control for comparison. The CT imaging *in vitro* was accomplished on Gamma Medica-Ideas. Imaging parameters were as follows: field of view, 1024 pixels × 1024 pixels; effective pixel size, 50 µm; 80 KV, 270 µA. The Hounsfield unit values and CT images *in vitro* were analyzed by using a Triumph™ X-O™ CT system. And the CT imaging *in vivo* was performed by using a SIEMENS CT imaging system (Inveon Gantry LG CT).

### Characterization

Transmission electron microscopy (TEM, Tecnai G<sup>2</sup> 20 S-TWIN) was employed to obtain the morphologies and size of the samples. The height of the samples was measured using atomic force microscopy (AFM, Agilent 5500, Agilent, USA). The crystal phase was obtained by using an X-ray powder diffractometer

(XRD, Japan Rigaku D/max-2500 diffractometer) with CuK $\alpha$  radiation ( $\lambda = 1.54056 \text{ \AA}$ ). Stability photographs were taken with a Nikon D3100 digital camera. The UV-vis absorption spectra were recorded on a UV-vis spectrophotometer (U3900, Hitachi). The temperature curve was recorded and infrared thermal images were taken by using a thermal imaging camera (E40, FLIR). Photoluminescence of SOSG was measured by using a fluorescence spectrophotometer (Horiba Jobin Yvon FluoroLog3). The luminescence microscopy images were taken by using an inverted luminescence microscope (OLYMPUS X-73, Japan).

## Results and discussion

The WS<sub>2</sub> nanosheets were synthesized *via* a liquid exfoliation method by using H<sub>2</sub>SO<sub>4</sub> intercalation and ultrasonication, which broke the van der Waals interaction forces in bulk WS<sub>2</sub> to give mono- and few-layer nanosheets (Scheme 1). Compared to previously reported Li ions insertion method for preparing WS<sub>2</sub> nanosheets,<sup>43</sup> the method presented here is insensitive to air and water and thus can potentially be scaled up to produce large quantities of exfoliated WS<sub>2</sub> nanosheets. AFM analysis (Fig. 1a) showed that the average thickness of as-obtained WS<sub>2</sub> nanosheets was about 1.6 nm, indicating the formation of mono- and few-layer nanosheets from WS<sub>2</sub> bulk. The crystal structure and



Fig. 1 AFM topography images of the as-made WS<sub>2</sub> nanosheets (a) and BSA-coated WS<sub>2</sub> (b). (c) TEM image of the as-synthesized WS<sub>2</sub> nanosheets. (d) XRD pattern of the as-obtained WS<sub>2</sub> nanosheets. (e) FT-IR spectra of WS<sub>2</sub> nanosheets (WS<sub>2</sub>), bovine serum albumin (BSA), and the BSA functionalized WS<sub>2</sub> nanosheets (BSA-WS<sub>2</sub>). (f) UV-vis spectra of the WS<sub>2</sub> nanosheets before and after BSA coating.



purity of the fabricated WS<sub>2</sub> were measured by XRD. As shown in Fig. 1d, all peaks exhibit the characteristics of the hexagonal WS<sub>2</sub> (JCPDS card no 08-0237). No other impurities were found, revealing the high purity of the as-obtained product. TEM images (Fig. 1c) confirmed the sheet like structure with diameters of 20–100 nm. In order to improve its bio-compatibility and dispersibility in physiological solutions, the as-prepared WS<sub>2</sub> was further functionalized with BSA through physical adsorption. After surface coating with BSA, the thickness of WS<sub>2</sub> nanosheets increased to 4–5 nm (Fig. 1b), mainly due to the attachment of BSA on both planes of WS<sub>2</sub> nanosheets. The FT-IR further confirmed the existence of BSA on the WS<sub>2</sub> nanosheets (Fig. 1e). The as-prepared BSA-WS<sub>2</sub> exhibited well dispersibility in PBS (Fig. S2†).

The aqueous solution of BSA-WS<sub>2</sub> showed a brown color with a strong absorption in the UV to NIR region (Fig. 1f). The

extinction coefficient of BSA-WS<sub>2</sub> nanosheets at 808 nm was determined to be  $21.8 \text{ L g}^{-1} \text{ cm}^{-1}$ , which was higher than that of Au nanorods (a commonly used PTT agent)<sup>18,21,26,46</sup>. Thus, this kind of nanoparticles has the potential as photothermal agents. Next, we evaluated the photothermal effect of WS<sub>2</sub> nanosheets at different concentrations upon irradiation at  $1 \text{ W cm}^{-2}$  with an 808 nm laser for 10 min (Fig. 2a). Pure water was used as the negative control. With the addition of WS<sub>2</sub> nanosheets, the temperature of the WS<sub>2</sub> contained solution increased with the irradiation time, and the temperature increased more rapidly with increasing concentrations of WS<sub>2</sub> nanosheets. For example, the temperature of the solution containing  $450 \mu\text{g mL}^{-1}$  WS<sub>2</sub> rose from  $25^\circ\text{C}$  to  $55^\circ\text{C}$  after NIR irradiation for 10 min. In contrast, the temperature of pure water only increased by  $2^\circ\text{C}$  under the similar experimental condition. Furthermore, we found that the photothermal heating effect of



Fig. 2 (a) Temperature evaluation of pure water and the aqueous dispersion of WS<sub>2</sub> nanosheets at different concentrations (12.5, 25, 50, 100, 300, 450 ppm) as a functional of irradiation time (0–10 min) using an 808 nm laser at a power density of  $1.0 \text{ W cm}^{-2}$  at room temperature. (b) Temperature evaluation of the aqueous dispersion of WS<sub>2</sub> nanosheets (50 ppm) as a functional of irradiation time (0–10 min) using an 808 nm laser at different power densities (0.3, 0.5, 0.8,  $1.0 \text{ W cm}^{-2}$ ), and pure water was used as the negative control. (c) Photothermal response of the aqueous dispersion of WS<sub>2</sub> nanosheets (50 ppm) under the NIR laser (808 nm,  $1.0 \text{ W cm}^{-2}$ ) irradiation for 13 min, and then the laser was shut off. (d) Linear time data versus  $-\ln \theta$  obtained from the cooling period of (d). (e) IR images of the WS<sub>2</sub> nanosheets solution before and after the 808 nm laser irradiation at a power density of  $1 \text{ W cm}^{-2}$  for 10 min.

WS<sub>2</sub> nanosheets was laser power intensity-dependent (from 0.3 to 1.0 W cm<sup>-2</sup>) (Fig. 2b). With the increase of the NIR laser power density, the temperature of the photothermal material became higher. The photothermal conversion efficiency ( $\eta$  value) was calculated to be 32.83% based on eqn (1) (ref. 47) (see ESI for details†).

$$\eta = \frac{hs(T - T_{\text{surr}}) - Q_{\text{Dis}}}{I(1 - 10^{-A_{808}})} \quad (1)$$

The  $\eta$  value of WS<sub>2</sub> is comparable to that of Au nanorods,<sup>22–25</sup> indicating that the as-prepared BSA-WS<sub>2</sub> was suitable for using as a PTT agent (Fig. 2c and d).

Considering its sheet like structure and the relevant high surface area, the WS<sub>2</sub> nanosheets are also expected to be drug carriers for drug delivery. In this work, for the first time, we used WS<sub>2</sub> nanosheets for loading and delivery of PSs for combined PDT and PTT. MB was chosen as the model PS because of its high photosensitizing efficacy and low dark toxicity.<sup>48</sup> The surface functionalization with BSA not only improves their dispersibility but also offers the capability to load MB on the surface of WS<sub>2</sub>. Due to BSA's amphiphilic molecular structure, it allowed tight adsorption of lipophilic PS molecules.<sup>49</sup> Thus, MB could be easily loaded onto the surface of WS<sub>2</sub> by a simple physical mixing. The saturated loading capacity for MB in PBS was determined to be 0.1 mmol g<sup>-1</sup> by measuring the characteristic absorption peak of MB at 665 nm (Fig. 3a). Therefore, it could be concluded that BSA-WS<sub>2</sub> has promising potential for PS delivery.

The release behavior of MB from WS<sub>2</sub> in PBS was also investigated and a low leakage within 10% of MB escaped from WS<sub>2</sub> after 24 h incubation was observed, revealing the good stability of these BSA-WS<sub>2</sub>@MB complexes for use in biological applications. Interestingly, the release of MB could be greatly accelerated by NIR irradiation. As shown in Fig. 3b, the NIR irradiation (808 nm, 1 W cm<sup>-2</sup>) apparently enhanced the cumulative release of MB at different time points, which could be ascribed to the photothermal effect of WS<sub>2</sub> nanosheets since increasing the local temperature would dissociate the interactions between MB and WS<sub>2</sub> nanosheets and thus more MB molecules are detached from the nanocarriers. For example, the cumulative release of MB with NIR irradiation was about 8-fold higher than that without NIR irradiation. That means the photothermal effect of WS<sub>2</sub> could finely control the release behavior of MB from WS<sub>2</sub> nanosheets.

The efficient generation of cytotoxic singlet oxygen plays a key role in photodynamic therapy. We thus investigated the singlet oxygen generation of the BSA-WS<sub>2</sub>@MB complex upon irradiation using a 665 nm LED lamp. The singlet oxygen sensor green (SOSG) was employed as the detector to measure the generation of singlet oxygen, which reacted irreversibly and caused an enhancement of SOSG fluorescence at 530 nm.<sup>2</sup> BSA-WS<sub>2</sub> only, free MB and BSA-WS<sub>2</sub>@MB complex were mixed with SOSG, respectively and then illuminated under 665 nm LED lamp excitation at different intervals. As shown in Fig. 3c, BSA-WS<sub>2</sub> only has no obvious ability to produce singlet oxygen since the fluorescence intensity of SOSG remained unchanged. In contrast, when free MB was exposed to the 665 nm LED lamp, a

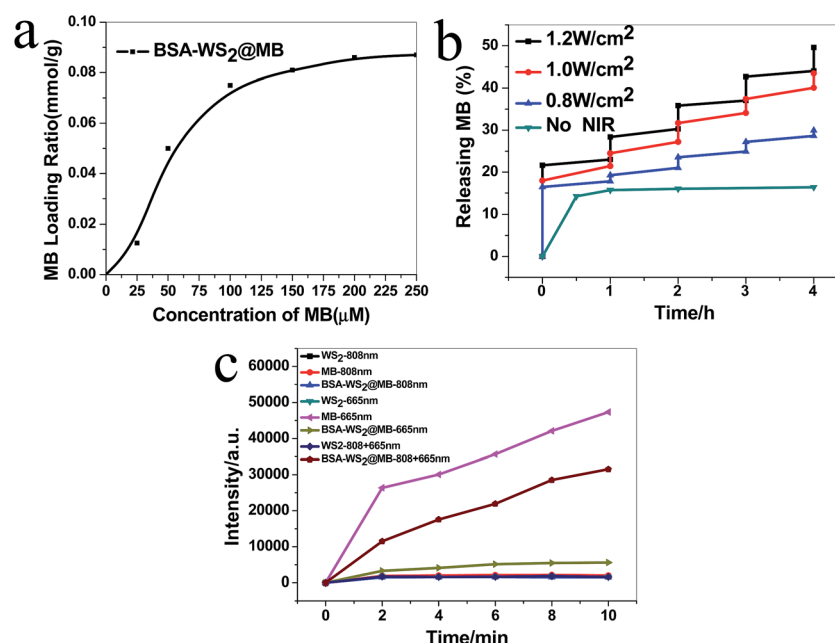


Fig. 3 Photosensitizer loading and releasing behavior. (a) Plots of the loading amount of the photosensitizer methylene blue (MB) on WS<sub>2</sub> nanosheets at different concentrations. (b) MB releasing from the MB-loaded WS<sub>2</sub> complex under the 808 nm laser irradiation at different output power densities (1.2, 1.0, 0.8 W cm<sup>-2</sup>, respectively). (c) The time-course generation of singlet oxygen by measuring the increase in the fluorescence intensity of SOSG at the characteristic peak of 530 nm as a functional of 665 nm LED lamp irradiation time. The output power density and irradiation time of the 808 nm laser for all samples were fixed at 1 W cm<sup>-2</sup> and 15 min, respectively. Irradiation by using the 665 nm LED lamp was carried out after the 808 nm irradiation treatment, and the power output of the 665 nm LED lamp for all samples was fixed at 50 mW cm<sup>-2</sup>.

significant increase in the emission intensity of SOSG was observed. BSA-WS<sub>2</sub>@MB also produced singlet oxygen but the amount was much lower than that of the free MB under similar conditions. The reason for this phenomenon may be that WS<sub>2</sub> could efficiently quench the singlet oxygen generation (SOG) of MB due to its high optical absorption and efficient energy transfer from MB to WS<sub>2</sub> nanosheets. Fortunately, the photoactivity of PSs could be restored by introducing the NIR irradiation. As shown in Fig. 3c, after irradiation using an 808 nm laser for 10 min, the SOG greatly enhanced since the intensity of SOSG increased 5-fold than that without NIR irradiation. These results inspired us in a way that the as-obtained BSA-WS<sub>2</sub>@MB complex could be employed as a smart platform for controllable singlet oxygen generation. During the delivery process, the singlet oxygen generation of MB adsorbed on the WS<sub>2</sub> surface was greatly inhibited. When these nanoparticles arrived at target tissues, the photoactivity of PSs was quickly recovered after introducing the NIR irradiation, which disturbed the interaction between MB and WS<sub>2</sub> nanosheets eventually resulting in the release of MB from WS<sub>2</sub>. This may improve the PDT selectivity to tumors while leaving healthy tissues unharmed. Moreover, the therapeutic efficacy of the BSA-WS<sub>2</sub>@MB complex could be further enhanced by addition of NIR induced PTT.

Before we move on to demonstrate the phototherapy effect of the BSA-WS<sub>2</sub>@MB complex, we evaluated the cytotoxicity characteristics of WS<sub>2</sub> before and after BSA coating, which is a very important issue towards medical applications of such

materials. The standard Cell Counting Kit-8 (CCK-8) assay was used to determine the relative cell viability of HeLa cells after they were incubated with WS<sub>2</sub> and BSA-WS<sub>2</sub> at various concentrations for 24 h (Fig. 4a). No significant cytotoxicity of WS<sub>2</sub> nanosheets was observed even at higher concentrations up to 0.2 mg mL<sup>-1</sup>, where the cell viability of HeLa cells is still higher than 85%. In contrast, the WS<sub>2</sub> nanosheets prepared by a Li ions insertion method have been reported to have obvious toxicity under the similar condition.<sup>43</sup> The reason for the lower toxicity of our obtained WS<sub>2</sub> nanosheets may be that we prepared these WS<sub>2</sub> nanosheets in a mild aqueous solution without using any toxic organic solvents and chemicals. Therefore, the strategy presented in this work is much 'green' for the fabrication of WS<sub>2</sub> nanosheets with low toxicity, benefiting their use in further bio-applications. BSA-coated WS<sub>2</sub> nanosheets also show very low toxicity since BSA molecules are well known for their biocompatibility.

Next, *in vitro* phototherapy effects of the PTT, PDT and combined PDT-PTT were evaluated by using HeLa cells. For PTT test, the cells were incubated with BSA-WS<sub>2</sub> for 2 h and then exposed to an 808 nm laser at 1 W cm<sup>-2</sup> for 10 min. After the treatment, the cell viability was determined using CCK-8. As presented in Fig. 4b, the cell viability gradually decreased with the increase of the laser power output, indicating the NIR-induced photothermal-killing of cancer cells. For the PDT effect evaluation, HeLa cells were incubated with BSA-WS<sub>2</sub>@MB and free MB for 2 h and then irradiated by using a 665 nm LED lamp at 50 mW cm<sup>-2</sup> for 3 min, respectively. The power and dosage of



Fig. 4 (a) Cell viability of HeLa cells incubated with WS<sub>2</sub> and BSA-WS<sub>2</sub> at various concentrations for 24 h without light interference, respectively. (b) *In vitro* cytotoxicity effect of WS<sub>2</sub> induced by PTT, showing that higher laser power density induces higher cytotoxicity. (c) *In vitro* cytotoxicity effect of PDT, PTT, and PTT + PDT. The output power of the 808 nm laser and 665 nm LED lamp for all tests was fixed at 1 W cm<sup>-2</sup> for 15 min and 50 mW cm<sup>-2</sup> for 5 min, respectively. Error bars were based on the standard deviation of six parallel samples. *P* values were carried out by Student's *t*-test: \* *P* < 0.05, \*\* *P* < 0.001.

the 665 nm light were very low and thus could not cause any obvious heating effect of WS<sub>2</sub>. Hence, the cell destruction is contributed by the PDT effect of the BSA-WS<sub>2</sub>@MB complex. As shown in Fig. 4c, upon 665 nm light excitation, the BSA-WS<sub>2</sub>@MB complex could kill the cancer cells but its efficacy is lower than that of free MB under the same condition since the WS<sub>2</sub> inhibits the singlet oxygen generation by its quenching effects as mentioned above. However, by introducing the 808 nm irradiation, the cancer cell killing ability of the BSA-WS<sub>2</sub>@MB complex was greatly enhanced, resulting in much lower cell viability compared to those after mono-therapy with 665 nm LED only treatment or with 808 nm laser only treatment. These results clearly confirm the enhanced therapeutic performance of the BSA-WS<sub>2</sub>@MB complex by combining both PTT and PDT. The reason for the enhancement of therapeutic efficacy may be that upon NIR irradiation, the photothermal effects of WS<sub>2</sub> accelerated the release of PS from carriers and then recovered the singlet oxygen generation of PSSs, resulting in improved PDT effects for killing cancer cells. Moreover, the photothermal effect caused by WS<sub>2</sub> nanosheets also enhanced the anticancer efficacy.

To further demonstrate the phototherapy effects of combined PTT-PDT treatment on cancer cells, intuitive visual results are obtained from the experiment using live-dead cell staining. As shown in Fig. 5, the survival status of HeLa cells has been illustrated by staining them with fluorescent dyes; green indicating live cells and red representing the dead ones. In the absence of WS<sub>2</sub> or MB, the 808 nm NIR laser and 665 nm LED light did not cause any obvious damage to cells. As shown in Fig. 5d, the PTT-only treatment could kill the cancer cells and its efficacy is little higher than that of the PDT-only effect (Fig. 5e).

The combined effects of PDT followed by PTT treatment, as illustrated in Fig. 5f, induced significantly higher cell death than the PDT-only or PTT-only treatment, indicating the enhanced efficiency of the combined therapeutic system. These results are well in agreement with the cell viability assay as mentioned above.

Because WS<sub>2</sub> nanosheets contained a high atomic number element (W ions) that has a strong X-ray attenuation ability, they could be used as an X-ray computed tomography (CT) imaging contrast agent. A series of CT images were obtained with 6 gradient concentrations of BSA-WS<sub>2</sub> dispersed in 0.5% agarose gel solution in the range of 0–10 mg mL<sup>-1</sup>. Iopromide (a commercially used CT contrast agent), at the same series of concentrations, was also used for comparison with the WS<sub>2</sub> nanosheets. As shown in Fig. 6a and b, with the increase of BSA-WS<sub>2</sub> concentrations, a sharp signal enhancement and a continuous increase of the CT numbers called Hounsfield units were clearly observed. We also found that the slope of Hounsfield units of BSA-WS<sub>2</sub> was about 36.19 HU L g<sup>-1</sup>, which was much higher than that of iopromide (20.10 HU L g<sup>-1</sup>) at the same concentration. Then, the CT imaging *in vivo* was also carried out by using BSA-WS<sub>2</sub> nanosheets to further evaluate its potential for using as a CT imaging agent. A Balb/c nude mice bearing HeLa tumors was intratumorally injected with BSA-WS<sub>2</sub> nanosheets (3 mg mL<sup>-1</sup>, 50  $\mu$ L) and imaged with a CT imaging system (SIEMENS, Inveon Gantry LG CT) (Fig. 6c). Strong signals from WS<sub>2</sub> at the tumor site were clearly observed from the CT image. Therefore, BSA-WS<sub>2</sub> is a promising candidate to be employed as a contrast agent in CT imaging.



**Fig. 5** Fluorescence images of HeLa cells incubated with (A) WS<sub>2</sub>, (B) BSA-WS<sub>2</sub>, (C) laser only (808 nm LED + 665 nm LED), (D) WS<sub>2</sub>@MB + 665 nm LED, (E) WS<sub>2</sub> + 808 nm laser, and (F) WS<sub>2</sub>@MB + 808 nm laser + 665 nm LED for 2 h after live-dead cell staining; Green indicates live cells and red represents the dead ones. The concentration of WS<sub>2</sub>@MB was fixed at 100  $\mu$ g mL<sup>-1</sup>. And the 808 nm laser (1 W cm<sup>-2</sup>) and 665 nm LED (50 mW cm<sup>-2</sup>) irradiation was carried out for 15 min and 5 min, respectively.



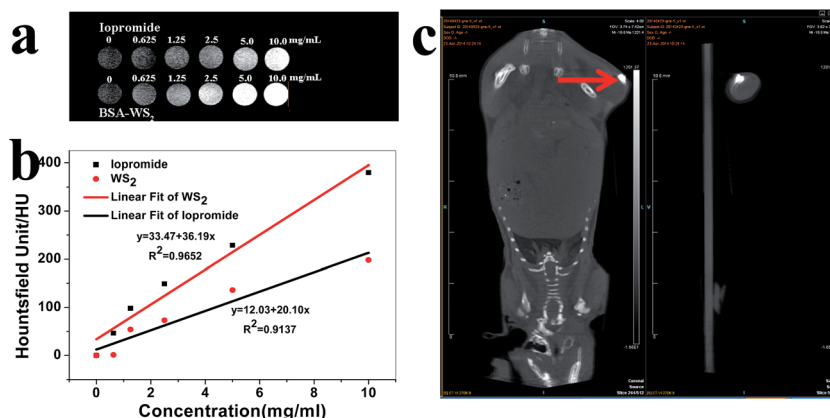


Fig. 6 (a) *In vitro* CT images of iopromide and BSA-WS<sub>2</sub> aqueous solutions at different concentrations. (b) Hounsfield unit values of BSA-WS<sub>2</sub> and iopromide as the function of their concentrations. (c) *In vivo* CT image of a Balb/c nude mouse after intratumor injection with 3 mg mL<sup>-1</sup> BSA-WS<sub>2</sub> nanosheets.

## Conclusions

In summary, we developed a facile and eco-friendly method to synthesize WS<sub>2</sub> nanosheets as a PTT agent. We are the first to employ these WS<sub>2</sub> nanosheets as drug carriers to load photosensitizer MB for combined PTT and PDT treatment of cancer cells. The as-prepared WS<sub>2</sub> nanosheets could not only efficiently load photosensitizers but also regulate their singlet-oxygen generation by NIR irradiation, making them a smart platform for the controllable regulation of photoactivity of PSs. The PDT, PTT and combined PTT-PDT effects of the WS<sub>2</sub> and BSA-WS<sub>2</sub>@MB complex were evaluated, and the efficacy of the combined PDT-PTT treatment of cancer cells is significantly higher than those of PDT-only and PTT-only treatments. This clearly shows that the WS<sub>2</sub> nanosheets could serve as a multi-therapeutic platform that combines different therapeutic modalities to realize the synergistic effect for cancer therapy. Moreover, the WS<sub>2</sub> nanosheets featuring strong X-ray attenuation also hold promise for CT imaging and thus may be approved as a multifunctional nanoplatform for simultaneous imaging-guided diagnosis and therapy.

## Acknowledgements

This work was supported by the National Basic Research Programs of China (973 program, no 2012CB932504, 2011CB933403 and 2013CB933704), and the National Natural Science Foundation of China (no 21177128, 21277037 and 21101158).

## References

- Z. G. Zhou, B. Kong, C. Yu, X. Y. Shi, M. W. Wang, W. Liu, Y. N. Sun, Y. J. Zhang, H. Yang and S. P. Yang, *Sci. Rep.*, 2014, **4**, 3653.
- L. Cheng, K. Yang, Y. Li, J. Chen, C. Wang, M. Shao, S. T. Lee and Z. Liu, *Angew. Chem., Int. Ed.*, 2011, **50**, 7385–7390.
- Z. M. Li, P. Huang, X. J. Zhang, J. Lin, S. Yang, B. Liu, F. Gao, P. Xi, Q. S. Ren and D. X. Cui, *Mol. Pharm.*, 2009, **7**, 94–104.
- W. Tang, H. Xu, R. Kopelman and M. A. Philbert, *Photochem. Photobiol.*, 2005, **81**, 242–249.
- G. Tian, W. L. Ren, L. Yan, S. Jian, Z. J. Gu, L. J. Zhou, S. Jin, W. Y. Yin, S. Li and Y. L. Zhao, *Small*, 2013, **9**, 1929–1938.
- K. H. Bae, M. Park, M. J. Do, N. Lee, J. H. Ryu, G. W. Kim, C. Kim, T. G. Park and T. Hyeon, *ACS Nano*, 2012, **6**, 5266–5273.
- P. Huang, Y. Kong, Z. Li, F. Gao and D. Cui, *Nanoscale Res. Lett.*, 2010, **5**, 949–956.
- D. Wen, *Heat Transfer Eng.*, 2013, **34**, 1171–1179.
- K. Pu, A. J. Shuhendler, J. V. Jokerst, J. G. Mei, S. S. Gambhir, Z. N. Bao and J. H. Rao, *Nat. Nanotechnol.*, 2014, **9**, 233–239.
- D. K. Kirui, I. Khalidov, Y. Wang and C. A. Batt, *Nanomedicine*, 2013, **9**, 702–711.
- A. Topete, M. Alatorre-Meda, P. Iglesias, E. M. Villar-Alvarez, S. Barbosa, J. A. Costoya, P. Taboada and V. Mosquera, *ACS Nano*, 2014, **8**, 2725–2738.
- I. Roy, T. Y. Ohulchanskyy, H. E. Pudavar, E. J. Bergey, A. R. Oseroff, J. Morgan, T. J. Dougherty and P. N. Prasad, *J. Am. Chem. Soc.*, 2003, **125**, 7860–7865.
- S. Kim, T. Y. Ohulchanskyy, H. E. Pudavar, R. K. Pandey and P. N. Prasad, *J. Am. Chem. Soc.*, 2007, **129**, 2669–2675.
- S. Wang, R. Gao, F. Zhou and M. Selke, *J. Mater. Chem.*, 2004, **14**, 487–493.
- D. Bechet, P. Couleaud, C. Frochot, M. L. Viriot, F. Guillemin and M. Barberi-Heyob, *Trends Biotechnol.*, 2008, **26**, 612–621.
- E. S. Nyman and P. H. Hynninen, *J. Photochem. Photobiol., B*, 2004, **73**, 1–28.
- P. Guardia, R. D. Corato, L. Lartigue, C. Wilhelm, A. Espinosa, M. Garcia-Hernandez, F. Gazeau, L. Manna and T. Pellegrino, *ACS Nano*, 2012, **6**, 3080–3091.
- H. J. Jang, Y. K. Kim, H. Huh and D. H. Min, *ACS Nano*, 2014, **8**, 467–475.
- J. Lin, S. J. Wang, P. Huang, Z. Wang, S. H. Chen, G. Niu, W. W. Li, J. He, D. X. Cui, G. M. Lu, X. Y. Chen and Z. H. Nie, *ACS Nano*, 2013, **7**, 5320–5329.
- Z. Fan, X. Dai, Y. Lu, E. Yu, N. Brahmbhatt, N. Carter, C. Tchouwou, A. K. Singh, Y. Jones, H. Yu and P. C. Ray, *Mol. Pharm.*, 2014, **11**, 1109–1116.

- 21 S. Khan, F. Alam, A. Azam and A. U. Khan, *Int. J. Nanomed.*, 2012, **7**, 3245–3257.
- 22 Y. Su, X. Wei, F. Peng, Y. Zhong, Y. Lu, S. Su, T. Xu, S. T. Lee and Y. He, *Nano Lett.*, 2012, **12**, 1845–1850.
- 23 B. Jang, J. Y. Park, C. H. Tung, I. H. Kim and Y. Choi, *ACS Nano*, 2011, **5**, 1086–1094.
- 24 Z. Zhang, J. Wang and C. Chen, *Adv. Mater.*, 2013, **25**, 3869–3880.
- 25 L. Gao, J. B. Fei, J. Zhao, H. Li, Y. Cui and J. B. Li, *ACS Nano*, 2012, **6**, 8030–8040.
- 26 J. Gautier, E. Allard-Vannier, E. Munnier, M. Souce and I. Chourpa, *J. Control. Release*, 2013, **169**, 48–61.
- 27 P. Huang, J. Lin, X. Wang, Z. Wang, C. Zhang, M. He, K. Wang, F. Chen, Z. Li, G. Shen, D. Cui and X. Chen, *Adv. Mater.*, 2012, **24**, 5104–5110.
- 28 X. Wang, C. Wang, L. Cheng, S. T. Lee and Z. Liu, *J. Am. Chem. Soc.*, 2012, **134**, 7414–7422.
- 29 X. Liu, H. Tao, K. Yang, S. Zhang, S. T. Lee and Z. Liu, *Biomaterials*, 2011, **32**, 144–151.
- 30 Z. Zhu, Z. W. Tang, J. A. Phillips, R. H. Yang, H. Wang and W. H. Tan, *J. Am. Chem. Soc.*, 2008, **130**, 10856–10857.
- 31 M. Zhou, R. Zhang, M. Huang, W. Lu, S. Song, M. P. Melancon, M. Tian, D. Liang and C. Li, *J. Am. Chem. Soc.*, 2010, **132**, 15351–15358.
- 32 Q. W. Tian, F. Jiang, R. J. Zou, Q. Liu, Z. G. Chen, M. F. Zhu, S. P. Yang, J. L. Wang, J. H. Wang and J. Q. Hu, *ACS Nano*, 2011, **5**, 9761–9771.
- 33 S. Ramadan, L. Guo, Y. Li, B. Yan and W. Lu, *Small*, 2012, **8**, 3143–3150.
- 34 Q. Tian, M. Tang, Y. Sun, R. Zou, Z. Chen, M. Zhu, S. Yang, J. Wang, J. Wang and J. Hu, *Adv. Mater.*, 2011, **23**, 3542–3547.
- 35 J. Hu, G. Song, L. Han, W. Zou, Z. Xiao, X. Huang, Z. Qin and R. Zou, *Nano-Micro Lett.*, 2014, **6**, 169–177.
- 36 Z. Zha, S. Wang, S. Zhang, E. Qu, H. Ke, J. Wang and Z. Dai, *Nanoscale*, 2013, **5**, 3216–3219.
- 37 Q. Xiao, X. Zheng, W. Bu, W. Ge, S. Zhang, F. Chen, H. Xing, Q. Ren, W. Fan, K. Zhao, Y. Hua and J. Shi, *J. Am. Chem. Soc.*, 2013, **135**, 13041–13048.
- 38 Y. Wang, H. Wang, D. Liu, S. Song, X. Wang and H. Zhang, *Biomaterials*, 2013, **34**, 7715–7724.
- 39 A. Sahu, W. I. Choi, J. H. Lee and G. Tae, *Biomaterials*, 2013, **34**, 6239–6248.
- 40 Y. Wang, K. Wang, J. Zhao, X. Liu, J. Bu, X. Yan and R. Huang, *J. Am. Chem. Soc.*, 2013, **135**, 4799–4804.
- 41 J. Oh, H. Yoon and J. H. Park, *Biomed. Eng. Lett.*, 2013, **3**, 67–73.
- 42 S. Wang, P. Huang, L. Nie, R. Xing, D. Liu, Z. Wang, J. Lin, S. Chen, G. Niu, G. Lu and X. Chen, *Adv. Mater.*, 2013, **25**, 3055–3061.
- 43 L. Cheng, J. Liu, X. Gu, H. Gong, X. Shi, T. Liu, C. Wang, X. Wang, G. Liu, H. Xing, W. Bu, B. Sun and Z. Liu, *Adv. Mater.*, 2014, **26**, 1886–1893.
- 44 T. Liu, C. Wang, X. Gu, H. Gong, L. Cheng, X. Shi, L. Feng, B. Sun and Z. Liu, *Adv. Mater.*, 2014, **26**, 3433–3440.
- 45 C. F. Zhu, Z. Y. Zeng, H. Li, F. Li, C. H. Fan and H. Zhang, *J. Am. Chem. Soc.*, 2013, **135**, 5998–6001.
- 46 J. Lin, S. J. Wang, P. Huang, Z. Wang, S. H. Chen, G. Niu, W. W. Li, J. He, D. X. Cui, G. M. Lu, X. Y. Chen and Z. H. Nie, *ACS Nano*, 2013, **7**, 5320–5329.
- 47 Q. W. Tian, F. R. Jiang, R. J. Zou, Q. Liu, Z. G. Chen, M. F. Zhu, S. P. Yang, J. L. Wang, J. H. Wang and J. Q. Hu, *ACS Nano*, 2011, **5**, 9761–9771.
- 48 J. P. Tardivo, A. D. Giglio, C. S. Oliveira, D. S. Gabrielli, H. C. Junqueira, D. B. Tada, D. Severino, R. F. Turchiello and M. S. Baptista, *Photodiagn. Photodyn. Ther.*, 2005, **2**, 175–191.
- 49 Q. Chen, C. Wang, L. Cheng, W. W. He, Z. P. Cheng and Z. Liu, *Biomaterials*, 2014, **35**, 2915–2923.